Physical modelling of tsunami onshore propagation, peak pressures, and shielding effects in an urban building array

Tori Tomiczek [a,*], Adi Prasetyo [b], Nobuhito Mori [b], Tomohiro Yasuda [c], Andrew Kennedy [a]

[a] University of Notre Dame, 156 Fitzpatrick Hall, Notre Dame, IN 46556, USA
[b] Kyoto University, Disaster Prevention Research Institute, Gokasho, Uji, Kyoto 6110011, Japan
[c] Kansai University, 3-3-35 Yamate-cho, Suita, Osaka 5648680, Japan

ABSTRACT

Wave experiments were conducted on a 1:20 length scale to measure water surface elevations and extreme pressures on and around idealized structural elements and arrays of structures. Experiments varied offshore wave characteristics and onshore structural configurations. Conditions in which waves broke on or just before the specimen caused maximum impulsive pressures. Pressures measured under nonbreaking wave conditions agreed with predicted values using design equations suggested by the Japanese Cabinet Office; however bare-earth water surface elevation inputs produced nonconservative estimates in breaking wave trials. Shielded structures experienced pressure reductions of 40–70% under breaking wave conditions. Results indicate that shielding elements constructed nearshore may reduce wave-induced damage. This dataset may be used to validate numerical models of tsunami propagation through urban environments.

© 2016 Published by Elsevier B.V.

1. Introduction

1.1. Coastal hazards

Coastal environments offer valuable sources of economy, transportation, and recreation, spurring a high concentration of people to settle near the coastline. The population density of coastal regions 100 km or closer to shore and within 100 m of sea level is over 2.5 times that of the global average, with the majority living in small coastal villages with <1000 people/km^2 (Nicholls and Small, 2002; Small and Nicholls, 2003). However, these communities are vulnerable to coastal hazards including tsunamis and hurricanes. In recent years, the 2004 Indian Ocean Tsunami (e.g. Papadopoulos et al., 2006; Tsuji et al., 2006; Koshimura et al., 2009; Leone et al., 2011) and the 2011 Tohoku Earthquake Tsunami in Japan (e.g. Mimura et al., 2011; Mori et al., 2011, Mori and Takahashi, 2012; Kazama and Noda, 2012; Udo et al., 2012; Kawai et al., 2013) caused extensive damage to coastal areas. Hurricanes and typhoons have also historically caused catastrophic damage and loss of life across the globe. Recent examples include Typhoon Haiyan (e.g. Tajima et al., 2014; Mori et al., 2014), Hurricane Sandy (e.g. Fanelli et al., 2013; Blake et al., 2013), and Hurricane Katrina (e.g. Robertson et al., 2007; van de Lindt et al., 2007). In the United States

alone, seven of the ten costliest disasters since 1980 have been caused by hurricanes (Lackey, 2011).

These coastal hazards emphasize the need to understand the fundamental processes causing damage in order to provide increased resilience to hurricane or tsunami events. However, on a local scale, engineers must consider site-specific characteristics to creatively employ hazard-mitigation methods that most effectively defend a particular community. Close to shore, a tsunami will be affected by the local bathymetry and tides, which can increase or decrease tsunami runup and inundation. As tsunamis approach shore, runup processes may be observed as a rushing bore or group of bores; for steeper beachfront slopes, a tsunami may cause a gradual rise and fall of the water level, and in some situations (e.g., the 1946 Aleutian Tsunami), a tsunami may form a collapsing breaker directly at the shoreline (Yeh, 2009). Seawalls, breakwaters, and vegetated dunes successfully or partially protected inland communities off the epicenter in the 2011 Tohoku Earthquake Tsunami and during Hurricane Sandy, while communities in other areas sustained near-complete destruction (Suppasri et al., 2013a; Nandasena et al., 2012; Irish et al., 2014). However, details of hydrodynamic transformation and forces as flows propagate through urban communities are still not well understood at both the research and design levels.

1.2. Previous tsunami and hurricane investigations

Common methods used to evaluate local conditions caused by tsunamis and hurricanes include post-disaster reconnaissance field

---

* Corresponding author.
  E-mail addresses: vtomicze@nd.edu (T. Tomiczek), adi.prasetyo246@yahoo.com (A. Prasetyo), mori@oceanwave.ac.jp (N. Mori), tomo@oceanwave.jp (T. Yasuda), Andrew.B.Kennedy.117@nd.edu (A. Kennedy).

surveys, numerical modelling, and laboratory experiments. After a tsunami or hurricane, field surveys are useful in assessing damage and measuring runup and high water marks (e.g. Mori et al., 2011). Such surveys have led to the development of empirical fragility models that relate inundation height, structural characteristics, and other hindcast variables to a structure's probability of damage (Suppasri et al., 2012, 2013b; Tomiczek et al., 2014, 2016). However, it is often difficult to estimate water velocities or forces on structures from post-disaster survey data. In addition to on-site surveys, numerical models such as ADCIRC (Luettich et al., 1992), SLOSH (Jelesnianski et al., 1992) for storm surge, SWAN (Holthuijsen et al., 1993) for wave spectral modelling, FUNWAVE (Wei and Kirby, 1995), COULWAVE (Lynett et al., 2008), and NHWAVE (Ma et al., 2012) for phase resolving wave modelling, have been developed to simulate hurricane conditions or tsunami propagation over local topographies. These models require validation and refinement to reliably predict overland wave dissipation. Often, numerical models remove structures and use land-use-based roughness coefficients rather than explicitly modelling the complex wave-structure interaction, leading to errors in model outputs (e.g. Westerink et al., 2008; Dietrich et al., 2012). Therefore, wave models, vulnerability assessments, and damage prediction techniques must be refined to account for wave interaction with individual structures and groups of structures to design resilient coastal communities.

Laboratory experiments are an essential starting point in understanding urban roughness effects on hydrodynamic phenomena. Historical experiments have provided valuable datasets that have been used to validate numerically-simulated water velocities and water surface elevations, as well as to derive empirical Manning's n or roughness coefficients (e.g. Goto and Shuto, 1983; Synolakis, 1987; Briggs et al., 1995; Liu et al., 1995; Chen et al., 2007; Baldock et al., 2009). Goto and Shuto (1983) determined Manning's n values for tsunami flow through various configurations of vertical cylinders; however, Manning's n values for tsunami flow through urban areas and forests have been found to be too small (Bricker et al., 2015). Other tests have focused on tsunami characteristics, as breaking wave solutions differ significantly from the nonlinear shallow water equations for nonbreaking waves. To simulate tsunami profiles during the 2004 Indian Ocean Tsunami that showed breaking initial wave fronts, Baldock et al. (2009) performed experiments to measure water surface elevations, water velocities, and wavemaker displacements for breaking tsunami wave conditions. These experiments were forced using solitary wave conditions at the O.H. Hinsdale Wave Research Laboratory at Oregon State University. Goseberg et al. (2013) presented a thorough review of the state-of-the-art of these and other tsunami generation techniques including that by piston-type paddle, dam break, vertical wave board motion, and pneumatic wave generation, as well as limitations of such models.

Recent tests have further investigated wave propagation through urban environments (e.g. van de Lindt et al., 2009; Cox et al., 2008; Goseberg and Schlurmann, 2012; Goseberg, 2013). Measurements by Thomas et al. (2015) and Irish et al. (2014) found that macro-roughness elements, defined herein as groupings or arrays of large scale obstacles like buildings, seawalls, or forested areas, lead to increased protection in wake areas where waves are reflected and flow is diverted. However, structures in narrow regions are subject to flow amplification and increased hydrodynamic forces. Experiments on scale models of real cities have also been used to validate numerical models. Cox et al. (2008) generated a dataset of tsunami flow over and around a 1:50 idealization of Seaside, Oregon and showed that both the COULWAVE (Lynett et al., 2002) and STOC-IC (Tomita et al., 2006; Tomita and Honda, 2009) numerical models were able to capture many features of flow. Park et al. (2013) compared these data with predictions of water velocity, free surface elevation, and momentum flux from the COULWAVE model (Lynett et al., 2002). Few physical models have further addressed the role of shielding in reducing tsunami-induced run-up and pressures on inland structures. Goseberg (2013) analyzed effects of beachfront developments on reducing the maximum run-up of sinusoidal waves, while the effects of low-height mitigation walls on forces induced by tsunami bores were evaluated by Al-Faesly et al. (2012). Thomas and Cox (2012) extended the work of Oshnack et al. (2009) to show that small seawalls generally reduced the maximum tsunami load on a specimen, although local pressures were sometimes increased. Thomas and Cox (2012) developed empirical formulas for predicting reduction factors for the maximum tsunami force based on the incident tsunami and in-situ seawall characteristics.

1.3. Remaining questions and experimental scope

While the abovementioned tests have been useful and indicate progress toward robustly and accurately modelling wave-structure interaction, all were performed with idealizations of the tsunami wave profile. Many experiments have modelled tsunamis using solitary waves (e.g. Cox et al., 2008; Thomas and Cox, 2012; Park et al., 2013); however, Madsen et al. (2008) showed that solitary waves may not be suitable representations of real-world mega tsunamis due to upscaling discrepancies in wavelengths and periods between model and prototype. Recent works are using alternative methods of wave generation to creatively address the issue of modelling tsunamis in the laboratory (e.g. Rossetto et al., 2011; Goseberg, 2013). For example, Rossetto et al. (2011) validated a pneumatic tsunami generator that is capable of creating solitary waves and leading-depression N-waves with large wavelengths; the wavemaker was able to reproduce a time record of the 2004 Indian Ocean Tsunami off the coast of Thailand. Goseberg et al. (2013) used a novel pump-driven wave maker that produced prolonged sinusoidal and leading-depression N waves with periods of 15–120 s, thus resulting in more realistic prototype tsunami durations. Experimental results compared well with outputs from a numerical model time series of a tsunami water surface elevation in 30 m depth. Bremm et al. (2015) similarly used this volumetric wavemaker to investigate the drag and inertial forces on an aluminum specimen caused by long, leading-depression waves. These waves show better agreement between model and prototype time scales; however, they still simplify the tsunami profile. Water surface measurements recorded by GPS buoys during the 2011 Tohoku Earthquake Tsunami showed complex profiles consisting of waves with shorter periods and sharp peaks embedded in a longer time scale water level rise (Kawai et al., 2012, 2013). Laboratory experiments simulating complex wave conditions may thus provide a clearer understanding of tsunami propagation in the presence of macro-roughness elements. The goal of the current experiment was to generate complex offshore wave conditions involving combinations of short- and long-period waves to characterize the effects of incident wave characteristics in changing hydrodynamic phenomena around varying structural configurations. Benchmark data was collected at Kyoto University on a 1:20 length scale physical model to address this question.

The remainder of this work is organized as follows: Section 2 describes the hydraulic flume, instrumentation, and experimental program. Results are presented in Section 3, and the effects of incident wave conditions and macro-roughness elements on changing the maximum pressure on an idealized structure are described. Section 3 also characterizes the tsunami waveforms recorded by GPS buoys during the 2011 Tohoku Earthquake Tsunami and compares those to waves created in the current experiment. Finally, Section 4 addresses successes and limitations of the hydraulic flume and areas for future research before highlighting major conclusions and offering engineering recommendations for damage mitigation.

2. Instrumentation and experimental conditions

2.1. Hydraulic wave flume

Experiments were conducted at Kyoto University's Hybrid Tsunami Open Flume in Ujigawa Laboratory (HyTOFU), which has dimensions

45 m × 4 m × 2 m high and a design water depth of 0.8 m. In this experiment all wave conditions were imposed on a constant water depth of 0.700 m. Fig. 1 depicts plan and profile views of the wave flume and shows the coordinate system used in analysis, with waves propagating in the positive *x*-direction from *x* = 0 at the wavemaker's origin. The *y*-coordinate system was defined from the west wall of the flume and oriented alongshore, and the *z*-axis was defined positive upwards from the bed of the flume. The flume bed and side walls were constructed of smooth concrete (Manning's *n* = 0.0013, ODOT, 2014), with two 4 m long glass panels installed in the side walls. Upon generation, waves propagated across the smooth concrete bed of length 14.05 m and then up a 7.95 m long 1:10 planar slope before reaching the flat beach surface elevated 0.095 m above the stillwater level, where structural elements were positioned. The planar slope and flat beach were made of iron and coated with an anti-rust paint. At the end of the flat beach, flow propagated into an open drain and into a side channel with dimensions 30 m × 4 m × 2 m high, which allowed water to be cycled during pumping conditions.

The 1:10 planar slope is representative of a steep beach profile and is similar to beachfront slopes reported by Reis and Gama (2010). While beachfront slopes as steep as 1:5 have been documented (McLachlan and Dorvlo, 2005), most real-world beaches can be characterized by gentler slopes between 1:50–1:200. Based on the flume dimensions, a length scale of 1:20 was chosen, and offshore water surface perturbation target heights were chosen to be between 0.4 and 0.5 m, corresponding with prototype wave heights of 8–10 m, similar to the maximum tsunami water levels in Miyako point (8.5 m), Ayukawa point (8.6 m), and Soma point (9.3 m) observed in eastern Japan during the 2011 Tohoku Earthquake Tsunami (Japanese Cabinet Office (JCO), 2011). The range of wave conditions generated in this experiment, combined with the flume bathymetry, created a variety of onshore runup conditions.

The flume is capable of three types of wave generation: a constant-flow pump, a mechanical piston, and a vertical discharge of a constant volume of water from a set elevation above the free surface. A pump with a 70 kW, 980 rpm motor discharges a constant flow from two 2 m × 0.2 m sized outlets at the bed to produce a slow increase in water level similar to that associated with a tsunami or a typhoon-induced storm surge. The maximum pumping capacity is 0.83 m³/s, with a maximum operating time of 1200 s. A piston-type, mechanical paddle with maximum stroke of 2.5 m and a maximum moving speed of 2.827 m/s is capable of generating a solitary wave with a maximum

height of 0.5 m, regular waves with heights up to 0.35 m, and irregular waves using the Bretschneider-Mitsuyasu, JONSWAP, or 5-Parameter spectral functions. The final method of wave generation involves dropping a constant volume of water from a set elevation above the free surface in a variation of the dam-break analogy, similar to a technique described by Chanson et al. (2003); however, this method was not used in the current experiment.

Individually, the wave generation mechanisms in HyTOFU can create breaking or nonbreaking waves similar to those generated in previous experiments (e.g. Cox et al., 2008; Thomas and Cox, 2012; Goseberg et al., 2013; Bremm et al., 2015). However, creative combinations of the mechanical and pumping generation mechanisms can create waves that resemble the recent complex tsunami traces observed after the 2011 Tohoku Earthquake Tsunami. A computerized-synchronization program of all three wave-generation mechanisms triggers the superposition of piston-generated waves onto the pump-generated flow after a specified duration. Inputs into the program include the desired pumping flow rate (0–0.83 m³/s), the target solitary wave height (0–0.5 m), and the duration of pumping flow before solitary wave generation. In this experiment, pump flow was generated for 180 s, and a mechanically-generated wave was superimposed over the pumping flow after 60 s. Table 2 shows the inputs into the synchronization program for mechanical target wave heights and pump flow rates for this experiment; seven combinations of inputs were tested to create a constant total offshore water surface perturbation with varying wave characteristics ranging from a strong constant flow to a nearly pure solitary wave.

2.2. Structural elements and pressure measurements

Acrylic and steel structural elements represented coastal residences. Based on the 1:20 experimental length scale, the dimensions of the structural elements (0.40 m × 0.40 m × 0.50 m high) correspond to a relatively narrow house that may be found in a typical Japanese coastal community (8 m × 8 m × 10 m high). The underside of the specimen was coated with a thin rubber mat (<1 mm thickness) and the specimen was weighted to the bottom using >100 kg weights. The specimen's location in the flume was marked to ensure that wave impact did not induce movement, though field surveys have noted that entire structures may be dislodged from their foundations and washed away during a tsunami (Gokon and Koshimura, 2012). Pressure sensors with a 50 kPa rated capacity were installed at elevations above the base of the structure 0.01 m, 0.05 m, and 0.15 m on the front, lateral, and back
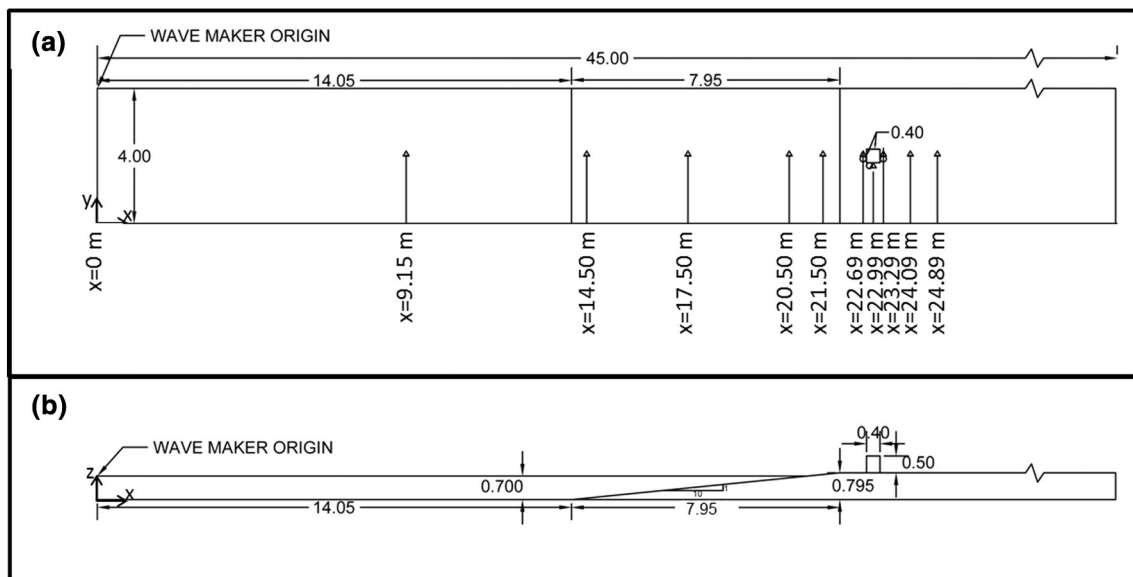

Fig. 1. (a) Plan and (b) profile views of experimental flume and wave gauge positions, with onshore locations as in Configuration 1. All dimensions are in meters.
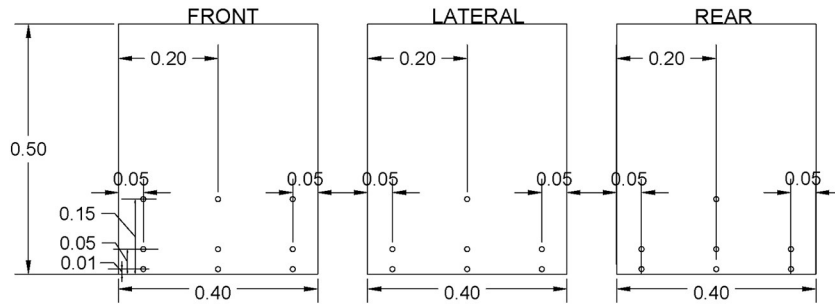
Fig. 2. Schematic of the front, lateral, and rear faces of the instrumented specimen, showing locations of pressure gauges. All dimensions are in meters.

sides of the instrumented specimen as shown in Fig. 2. Fig. 3 shows a photograph of wave gauges and Acoustic Doppler Velocimeters (ADVs) installed in the flume, as well as a frontal view of the instrumented specimen with mounted pressure gauges and a nearby wave gauge and ADV.

Pressure time series were recorded at a frequency of 200 Hz and cleaned to remove contamination by local utility frequencies (60 Hz) using a low pass filter for frequencies <50 Hz. Cleaned data was checked for sensitivity to frequency components; filtered and unfiltered peak pressure recordings differed by <5%. A sample time series of the pressure measured 0.01 m above the base of the structure on the centerline of each of the front, lateral, and rear faces of the instrumented specimen is shown in Fig. 4 for Trial 7, with the obstacle positioned 2.39 m from shore. The wave induces peaks in the frontal pressure time series; the first peak corresponds with the short-duration impact of the wave, and the second peak is due to the quasi-hydrostatic pressure exerted by the standing wave, as has been observed in previous experiments (e.g. Fujima et al., 2009; Bradner et al., 2009; Thomas and Cox, 2012). While other tests focusing on the pressure impulse have successfully used higher sampling rates between 400 and 10,000 Hz (e.g. Wood et al., 2000; Bullock et al., 2007), Cooker (2002) reported that at full scale the main pressure impulse typically lasts ~100 ms. For a 1:20 length scale and Froude similarity, the frequency used in experiments was enough to capture the duration of the main pressure spike, which at model scale would be predicted to last 0.022 s. In the current experiments, sensitivity tests run using recording frequencies of 500 Hz and 1000 Hz indicated that a sampling frequency of 200 Hz was sufficiently able to capture the pressure spike due to the impulsive wave load while optimizing the operation of the recording software. Wave-induced pressure impulse is a subject of active research, and has been difficult to characterize; the impulsive pressure itself has been shown to be

sensitive to the wave shape immediately before impact (Oumeraci et al., 1993; Hattori et al., 1994; Cooker and Peregrine, 1995; Peregrine, 2003). Wood et al. (2000) found that the compressibility of entrained air in breaking waves can affect wave-structure dynamics and the maximum pressure. Bullock et al. (2007) analyzed conducted pressure impulse experiments on a 1:4 physical model and distinguished between low aeration impacts, with short durations and high pressure spikes, and high aeration impacts, with longer durations and less localized pressure peaks. While at large scales aeration can affect the maximum impulsive pressure, for the smaller length scales of these experiments aeration effects become small. The pressure impulse, defined as the integral of the pressure time series over the duration of the impulsive pressure spike, has shown less sensitivity to the incident wave shape (Cooker and Peregrine, 1995; Cooker, 2002; Peregrine, 2003); however the scope of this paper focuses on the single maximum recorded pressure, which can be integrated to estimate the load on the face of the experimental specimen. For all experiments, the maximum pressure was recorded by a frontal pressure gauge, typically due to the wave impact. Bradner et al. (2009) noted that for large bridges the high amplitude of these pressure spikes may not be felt by structural supports due to the short duration of impact and the large inertia of the test specimen. However, this impact pressure can cause significant localized damage and cannot be neglected. Thus, the present analysis defined the critical pressure as the maximum pressure recorded on the front face of the structure.

2.3. Surface elevation measurements

Wire resistance wave gauges recorded the time series of water surface elevation ($\eta_{wave} + \eta_{flow}$) above the local initial water depth at varied locations along the flume, where η_{wave} and η_{flow} are the water
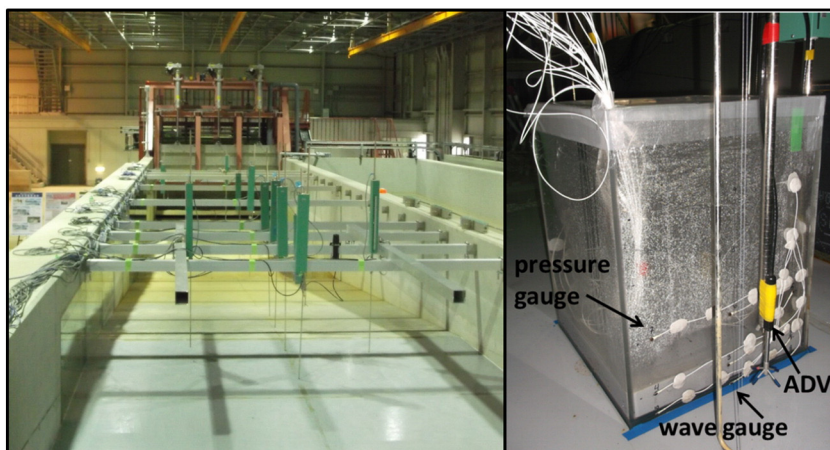

Fig. 3. Photographs of wave flume and instrumentation. Left: resistance wave gauges and ADVs positioned in hydraulic wave flume. Right: instrumented specimen and front-side pressure gauges, wave gauge, and ADV.
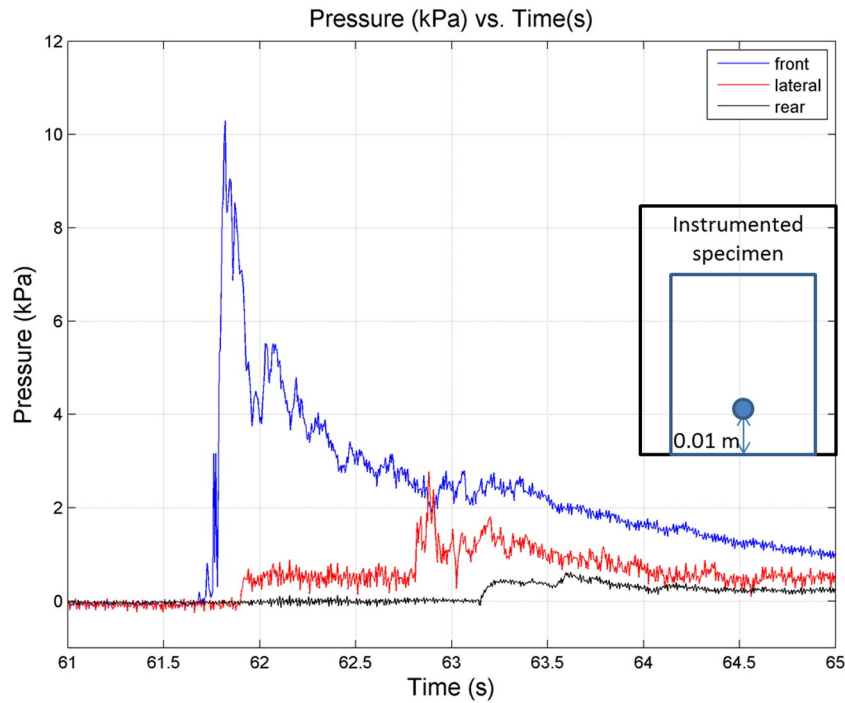
Fig. 4. Pressure time series for Trial 7, Configuration 3, on the front (blue line), lateral (red line), and rear (black line) pressure sensors, mounted along the structure's centerline at elevation $z = 0.01$ m. Inset: location of depicted pressure time series on the front, lateral, and rear sides. Time is measured from onset of pumping flow. (For interpretation of the references to colour in this figure legend, the reader is referred to the web version of this article.)

surface elevation increases generated by the mechanical paddle and pumping flow mechanisms, respectively. Stationary offshore wave gauges, WG1–WG5, were positioned along the centerline of the flume with distances from the mechanical paddle's origin shown in Fig. 1. These gauges were used to define wave characteristics and to check the repeatability of the wave form. Onshore wave gauges, WG6–WG10, were moved for each experimental configuration; these wave gauges were positioned 0.10 m from the front, lateral, and rear faces of the instrumented structural element. Figs. 5 and 6 show the nine experimental configurations tested, and Table 1 provides the x-locations
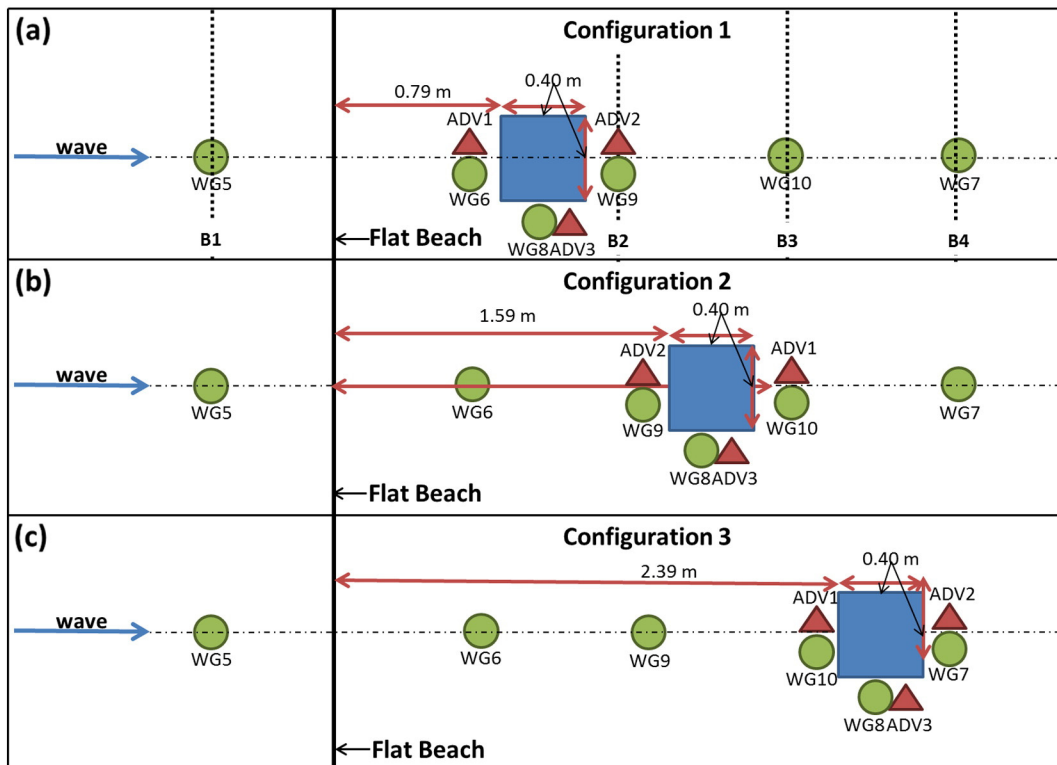

Fig. 5. Unobstructed structural element configurations with associated wave gauges and ADV locations: (a) Configuration 1, (b) Configuration 2, and (c) Configuration 3.
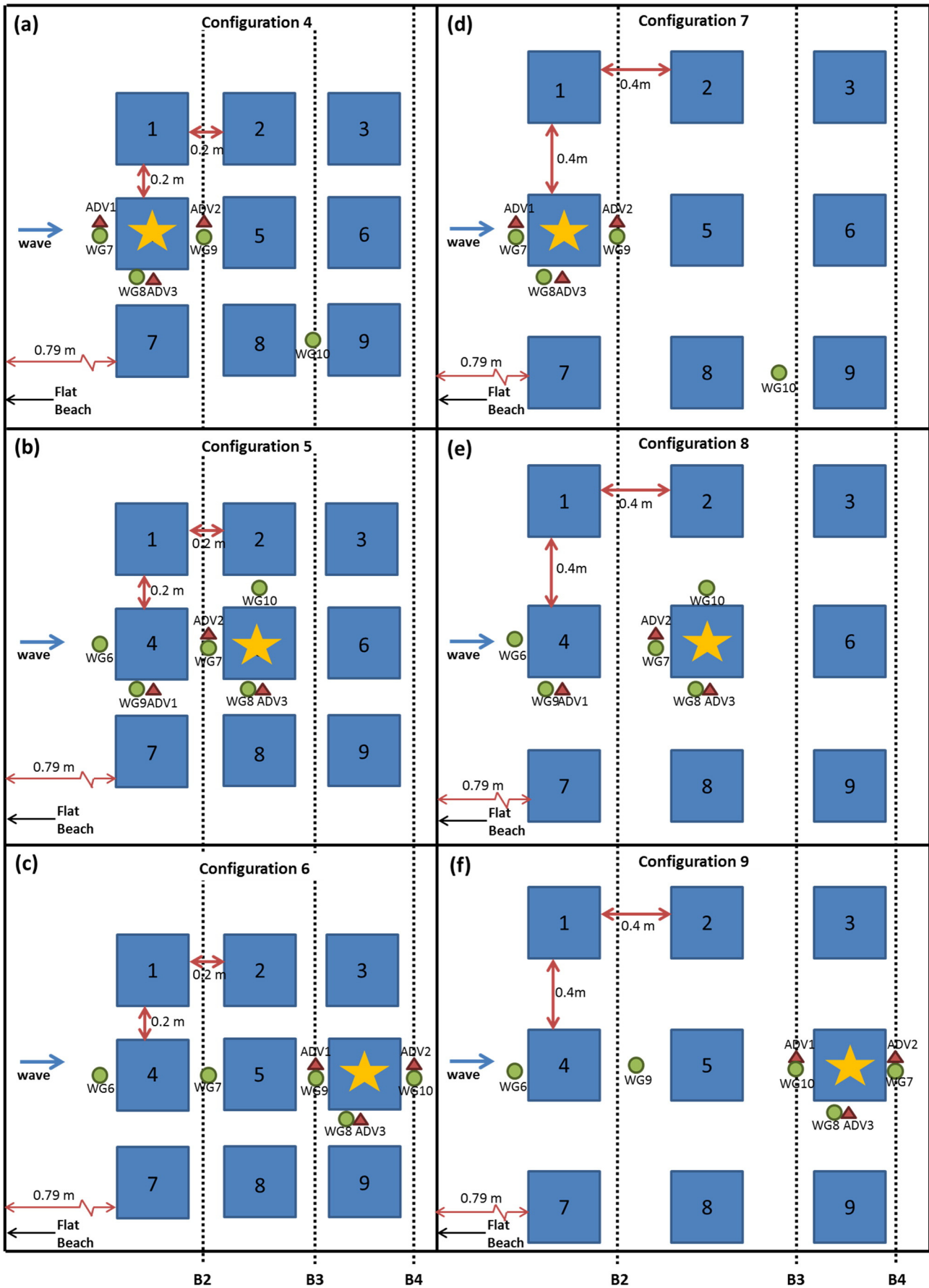
Table 1
Wave gauge positions (distance in meters from the origin of the mechanical paddle).

Config.	L (m)	x_{box} (m)	WG5	WG6	WG7	WG8	WG9	WG10
1	0.79	22.79	21.50	22.69	24.89	22.99	23.29	24.09
2	1.59	23.59	21.50	22.69	24.89	23.79	23.49	24.09
3	2.39	24.39	21.50	22.69	24.89	24.59	23.49	24.29
4	Front, a = 20 cm	22.79	21.50	n/a	22.69	22.99	23.29	23.89
5	Middle, a = 20 cm	23.39	21.50	22.69	23.29	23.49	22.99	23.49
6	Rear, a = 20 cm	23.99	21.50	22.69	23.29	24.19	23.89	24.49
7	Front, a = 40 cm	22.79	21.50	n/a	22.69	22.99	23.29	24.19
8	Middle, a = 40 cm	23.59	21.50	22.69	23.29	23.79	22.99	23.79
9	Rear, a = 40 cm	24.39	21.50	22.69	24.89	24.59	23.29	24.29

Table 2
Summary of initial conditions and offshore water surface elevations at x = 14.50 m. Experiments were run for each of the nine setback and spacing configurations. Mechanical waves were generated after 60 s of pump flow.

Trial	Mechanical input (m)	Pump input (m³/s)	$(\eta_{wave} + \eta_{flow})_{avg}$ (cm) x = 14.50 m	Standard deviation (cm)
1	0	0.80	43.19	1.72
2	0.10	0.60	43.08	1.33
3	0.15	0.40	40.74	0.71
4	0.20	0.30	40.76	0.41
5	0.25	0.20	39.63	0.15
6	0.35	0.10	41.94	0.15
7	0.40	0.10	47.71	0.18

of onshore wave gauges for each configuration. The flow velocity was recorded using four Nortek Vectrino ADVs installed within the array of structural elements and offshore at $x = 17.50$ m (see Figs. 5 and 6). However, ADV measurements, especially onshore ADV data, were affected by low water levels and breaking-wave turbulence. Therefore, the wave signal was often difficult to extract from noise, and velocity measurements are not considered in the present analysis.

2.4. Experimental conditions

Table 2 lists the seven combinations of wave conditions that were imposed on each of the nine configurations of structural elements. In all trials, the mechanically-generated wave was generated 60 s after the onset of pumping flow. For clarity, the remainder of the paper designates each combination of inputs as a "trial", while a specific wave condition generated across a specific configuration is termed "test". Input wave conditions were selected to generate an almost constant offshore total perturbation above the initial stillwater depth of 0.700 m with varying contributions due to the mechanical wave (η_{wave}) and constant flow (η_{flow}). Offshore water surface profiles for WG1–WG5 for both tests run in all trials for configuration 3, as well as definitions of η_{wave} and η_{flow}, can be seen in Fig. 7. For increasing mechanical waves, the height of the solitary wave relative to the total water surface perturbation increased for all offshore wave gauges; however, with the exception of Trial 7, increased mechanical wave inputs were paired with decreased pumping flow inputs to generate similar maximum offshore water surface elevations. Two tests were conducted for each trial-configuration combination to check the repeatability of the wave profile. For each of the 18 tests conducted for each trial, the ensemble average of the total water surface perturbation at WG2, positioned near the toe of the sloping beach is listed in Table 2. The total offshore water level perturbation was typically between 0.40 and 0.43 m; Trial 7 resulted in offshore perturbations about 15% larger than those generated in other trials. Based on the length scale used during experiments, offshore water surface elevations correspond to prototype scale perturbations 8–9.5 m above the mean water depth. Tests were conducted 15–20 min apart to allow the water surface to calm and to dry the flat beach and structural elements using squeegees and towels. Table 2 shows that for each trial, $(\eta_{wave} + \eta_{flow})$ measurements were repeatable for all configurations; standard deviations of water surface elevation records between repeated tests were between 0.0015 and 0.0172 m, much smaller than the wave signal. The slightly larger standard

deviation in the water surface profiles for trials with larger pumping inputs are due to greater wave reflection in Trials 4–9.

3. Results and discussion

3.1. Offshore wave characterization

Initial analysis examined the effects of the ratio of the solitary wave height (η_{wave}) to the total water surface perturbation due to the pumping flow and mechanical wave ($\eta_{wave} + \eta_{flow}$). The inputs from Trials 1–7 in Table 2 increased the amplitude of the solitary wave with respect to the constant flow water surface increase; for unobstructed configurations, the obstacle's setback distance from shore was also varied. These variations affected wave breaking characteristics with respect to the instrumented specimen, which changed the maximum pressure on the front face of the unobstructed obstacle for each setback configuration. Pressure was nondimensionalized using either the hydrostatic pressure of the offshore disturbance or the local, bare-earth water surface elevation recorded in a control, zero-obstacle configuration:

$$p_i^* = \frac{p_i}{\rho g \left(\eta_{wave,i} + \eta_{flow,i} \right)_{max}}, \tag{1}$$

or

$$p_i^{**} = \frac{p_i}{\rho g \left(\eta_{be,i} \right)_{max}}. \tag{2}$$

In Eqs. (1) and (2), p_i^* is the nondimensionalization of the measured pressure p_i at time step i using the offshore water surface perturbation at WG2 ($\eta_{wave} + \eta_{flow}$) and p_i^{**} is the nondimensionalization using the bare-earth water surface elevation at the location of the structure (η_{be}). Other variables in the above equations are the density of water, ρ, taken as 1000 kg/m³ for freshwater used in experiments, and the gravitational acceleration, g. Nondimensionalization of pressure using the different water surface elevations reflects different wave properties. The offshore water surface elevation characterizes wave conditions before waves are affected by shoaling or macro-roughness elements, while the local bare-earth water depth is a common parameter output by numerical models and used to estimate maximum pressures and loads in design guidelines (e.g. JCO, 2005; ASCE, 2016).

Wave characteristics at WG2 were also used to parameterize incoming waves. These incident signals of offshore waves may be readily reproduced by models, and thus may be used to simulate experiments for future studies. Understanding how offshore wave characteristics

Fig. 6. Experimental configurations with macro-roughness elements. (a, b, and c) Configurations 4, 5, and 6 (0.20 m spacing); (d, e, and f) Configurations 7, 8, and 9 (0.40 m spacing). Instrumented specimen is designated with a star for each configuration. The x-distances of wave gauges from the mechanical paddle are given in Table 1. Front and rear ADVs and wave gauges were positioned 0.10 m from the face of the instrumented structural element and at the midpoint between non-instrumented obstacles. Lateral ADVs were positioned 0.15 m behind the leading edge and 0.10 m to the side of the nearest structural element; lateral wave gauges were positioned 0.10 m behind the leading edge and 0.20 m to the side of the structural element.
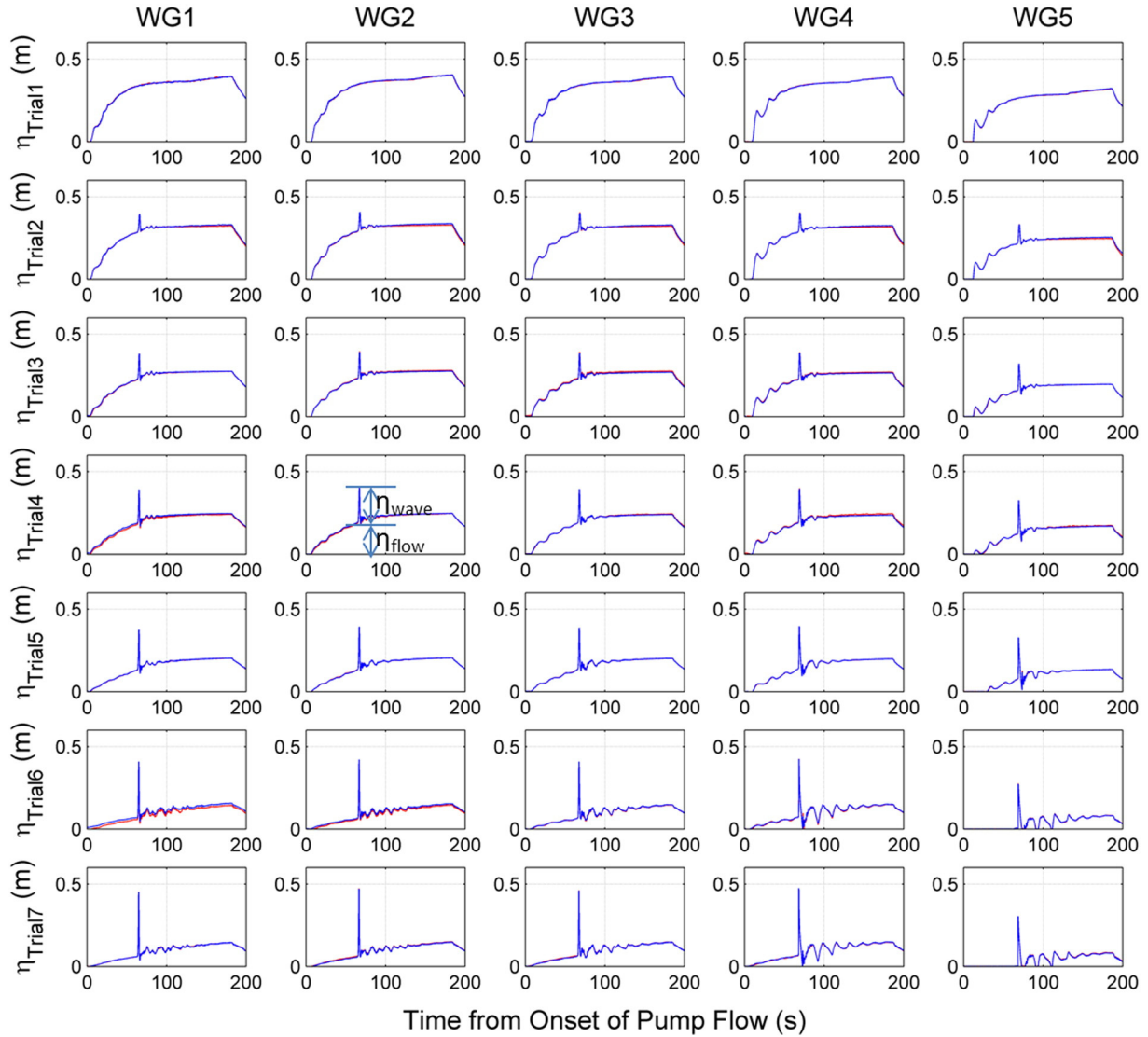
Fig. 7. Water surface time series for WGs 1–5 for each of the seven combinations of pumping flow rates and mechanical wave target inputs listed in Table 2. Time is measured from the initiation of pump flow.

affect onshore wave behavior is of significant interest for structural design. Additionally, these conditions are comparable to data recorded by offshore buoys during the 2011 Tohoku Earthquake Tsunami (NOWPHAS, 2011). In experimental analyses, the water surface perturbation generated by pumping flow, η_{flow}, above the local stillwater depth was recorded at the time just before the quick rise caused by the mechanically-generated wave. The solitary wave perturbation, η_{wave}, was then calculated by subtracting η_{flow} from the maximum recorded water surface perturbation; Fig. 7 shows the definitions of η_{flow} and η_{wave} for Trial 4. The ratio of η_{wave} to the total water surface perturbation, $\eta_{total} = (\eta_{wave} + \eta_{flow})$ was defined as the solitary wave fraction, η^*:

$$\eta* = \frac{\eta_{wave}}{\eta_{wave} + \eta_{flow}}. \tag{3}$$

Therefore, $\eta^* = 0$ for a constant flow with no superimposed solitary wave, while $\eta^* = 1$ for a solitary wave with no initial increase in water level.

Although η^* can be readily defined for this experiment, the choice of η^* depends on the somewhat arbitrary designation of η_{flow}. Therefore, surge conditions and definitions require further discussion, particularly

for field applications. A dimensionless rise time ratio, t^*, comparing the periods of the slow and fast rise waves, was thus introduced as an additional parameterization of η^*:

$$t^* = \frac{t_{slow}}{t_{total}}. \tag{4}$$

In the above definition, t_{slow} measures the time from the beginning of the tsunami signal, t_0, to the local peak due to the slow water surface rise, and t_{total} measures the time from t_0 to the maximum water surface elevation. Trial 1 involved only pump-generated flow; therefore, $\eta_{flow} = \eta_{total}$ and $t_{slow} = t_{total}$, so $\eta^* = 0$ and $t^* = 1$. For all other experimental conditions, η_{flow} was generated for 60 s after the start of the experiment (t_0) before the mechanical wave was produced, and the mechanical wave was recorded by WG2 shortly after its generation. The fast rise time was relatively consistent for the solitary wave, so t_{slow} was only a few seconds shorter than t_{total}. Because of these experimental controls, t^* was almost constant for offshore wave gauges (WG1, WG2, WG3, and WG4) across all trials ($t^*_{avg.} = 0.972$). Variations in flow rate were not reflected in experimental t^* calculations.

Note that the slow rise time and total rise time of a real tsunami may be expected to vary depending on an earthquake's rupture

Table 3
GPS buoy locations and wave characteristics during the March 11, 2011 Tohoku Earthquake Tsunami.

WG	η^*	t^*	Latitude (°N)	Longitude (°W)	Location	Depth (m)
GB807	0.897	0.486	40.117	142.067	N. Iwate	125
GB804	0.784	0.604	39.627	142.187	C. Iwate	200
GB802	0.660	0.682	39.259	142.097	S. Iwate	204
GB803	0.379	0.834	38.858	141.894	N. Miyagi	160
GB801	0.179	0.905	38.233	141.684	C. Miyagi	144
GB806	0.619	0.588	36.971	141.186	Fukushima	137

characteristics, causing more variation in t^* in the field than in the present experiment. Therefore, t^* and η^* were determined for the tsunami waveforms recorded by GPS buoys GB801, GB802, GB803, GB804, GB806, and GB807 during the Tohoku Earthquake Tsunami on March 11, 2011 (NOWPHAS, 2011). Table 3 provides the location and depth for each field gauge, and Fig. 8 shows the water surface profiles and the methodology for determining t^* and η^*. The initial time at which the water surface began to rise varied for each GPS buoy; therefore, t_0 was identified as the trough in the water surface profile before the slow and quick rises in the tsunami waveform. To determine the local peak and the onset of the quick rise wave, η_{flow} was defined to be consistent with analyses performed on these data by Kawai et al. (2013). Kawai et al. (2013) characterized the tsunami waveform at these buoys by considering the ratio of the elevation of a local peak occurring

after a slow rise, h_l to the height of the total wave crest, h_w. This ratio is essentially the complement of η^* defined here:

$$\eta* = \frac{\eta_{wave}}{\eta_{total}} = 1 - \frac{\eta_{flow}}{\eta_{total}} = 1 - \frac{h_l}{h_w}. \tag{5}$$

Calculations of η^* and t^* were made for each buoy and are plotted with experimental data from WG1, WG2, WG3, and WG4 in Fig. 9. As shown in Fig. 9, field gauges show a generally decreasing trend in t^* with increasing η^*, with GB801 recording a dimensionless rise time very similar to those generated in experiments. For a given tsunami event, the ratio of slow rise time to fast rise time will affect the solitary wave ratio. The variation of t^* and η^* with location for the Tohoku Earthquake Tsunami traces suggests that the rate of slow water level increase was relatively consistent for all latitudes; therefore, t^* may give insight into wave and flow characteristics when t_0 is varied. The decreasing trend of t^* with η^* for a given event makes intuitive sense: as the tsunami profile approaches a solitary wave ($\eta^* = 1$), there should be no slow rise before the initial crest; hence t_{slow} and thus t^* approach 0. Likewise, for a purely constant slow-rise increase ($\eta^* = 0$), t_{slow} approaches t_{total}, making t^* approach 1. Note that for GPS buoys north of 38° N latitude, η^* increased and t^* decreased with increasing latitude. Comparisons with runup and inundation data obtained by Mori and Takahashi (2012) indicated that the northern buoys GB802, GB804, and GB807, which recorded $\eta^* > 0.6$, were offshore of regions that experienced the highest
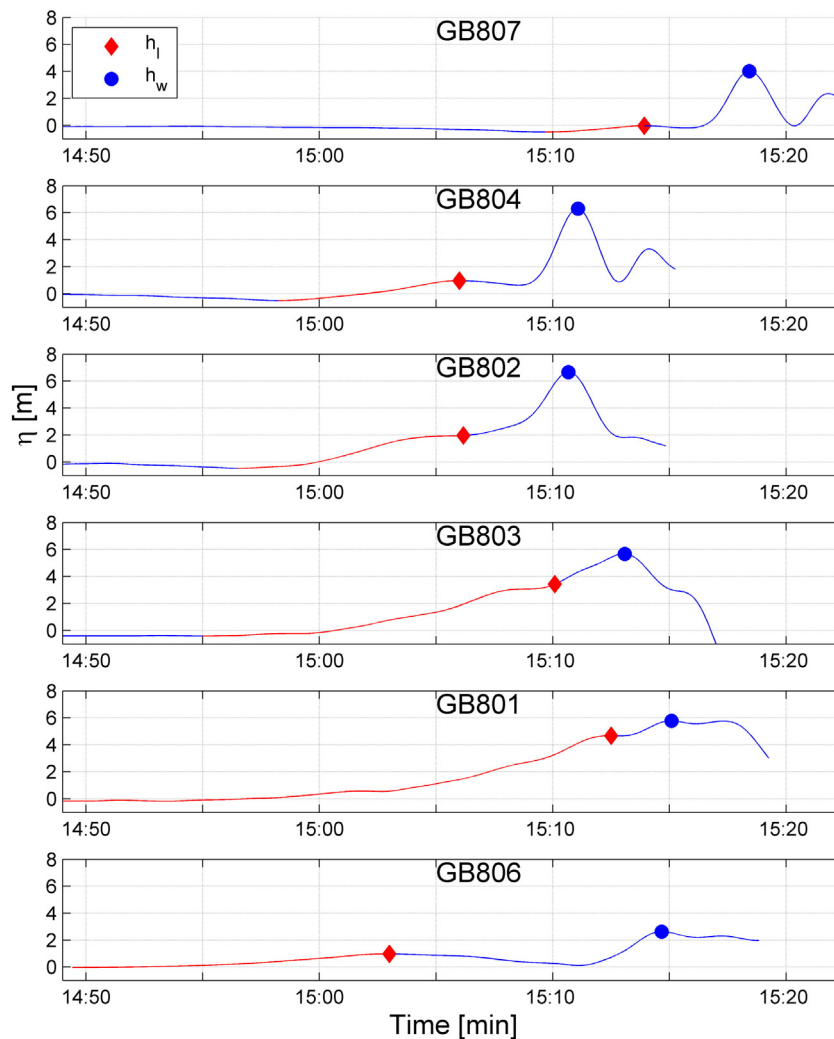

Fig. 8. Water surface elevation vs. local time and methodology for calculating t* and η* using NOWPHAS (2011) wave gauge data. Slow rise time t$_{slow}$ is shown in red over the blue water surface elevation time series. (For interpretation of the references to colour in this figure legend, the reader is referred to the web version of this article.)
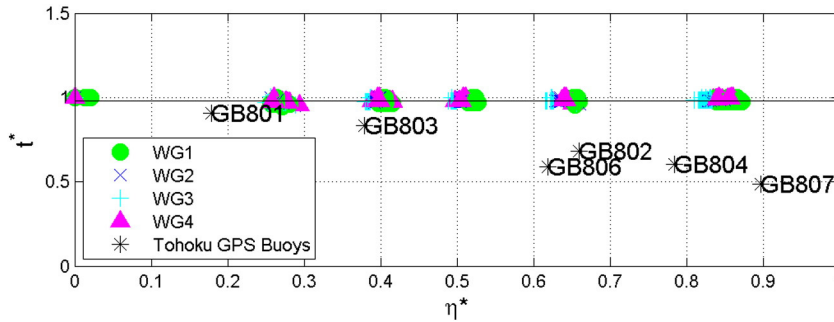
Fig. 9. Relationship between t* and η* for flume WG data and tsunami profiles obtained by GPS Buoys after the 2011 Tohoku Earthquake Tsunami.

measured tsunami runup and inundation heights. Local bathymetry and topography certainly affected tsunami runup and inundation; additionally, the flume geometry and availability of field data caused a discrepancy between prototype and model water depths. However, the offshore wave gauge data in the flume may cautiously be compared with these field data as the wave was not affected by the flume slope at measurement locations, and general trends may be compared to prototype effects. For example, this analysis may indicate that an offshore solitary wave ratio above 0.6 corresponds with more severe onshore tsunami effects. Such characterizations must be tested under other experimental conditions and in analyses of other field data or numerical model outputs to further examine the effects of varying t* and η*.

3.2. Solitary wave ratio effects on pressure

Fig. 10 depicts the relationship between p^*, p^{**}, and η* for each setback distance, and Table 4 presents the elevation of the pressure gauge which recorded the maximum pressure. Trials with large pumping inputs and small mechanical wave inputs corresponded with low values of η* and were observed to propagate past the obstacle as

nonbreaking waves for all setback distances. As seen in Fig. 10a, these trials showed a near 1:1 agreement between the maximum pressure and the nearshore hydrostatic pressure caused by the wave and flow perturbation. The largest pressure was recorded by a pressure gauge positioned near the base of the structure, indicating that hydrostatic pressures may dominate for nonbreaking waves.

In contrast to nonbreaking conditions, waves that broke on or just in front of the obstacle significantly changed the magnitude and location of maximum pressure recordings. Breaking was confirmed visually during experiments and with video recordings. In particular, for unobstructed configurations, the waves of Trials 6–7 were observed to break just before the flat beach. The wave generated in Trial 5 broke almost directly on the specimen positioned $L_1 = 0.79$ m from shore, while the wave of Trial 4 broke just before the specimen positioned at setback distance $L_2 = 1.59$ m. Trials 1–3 propagated unbroken past the obstacle at all three setback distances. Extreme pressures were recorded when waves broke directly onto or very close to the instrumented specimen; as an example, consider in Fig. 10a the wave of Trial 4, with offshore solitary wave fraction η* = 0.51. This wave propagated unbroken past the specimen positioned at $L_1 = 0.79$ m, the closest setback configuration.
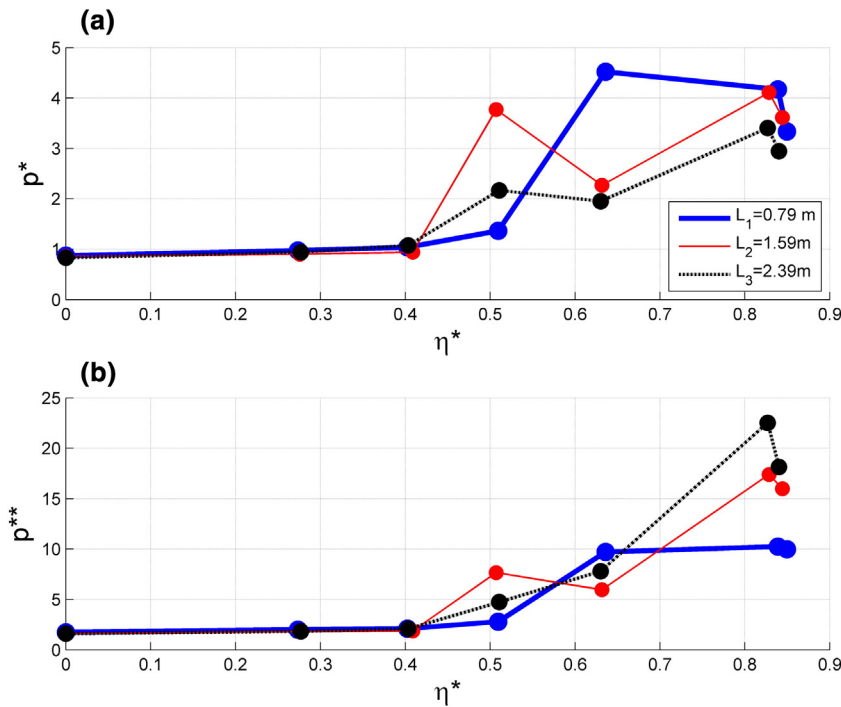

Fig. 10. Maximum front pressure, nondimensionalized by (a) total offshore water surface perturbation ($\eta_{wave} + \eta_{flow}$) and (b) local bare-earth water surface elevation (η_{be}) vs. offshore solitary wave fraction, unobstructed configurations. Setback distances are $L_1 = 0.79$ m (blue, bold line), $L_2 = 1.59$ m (red, thin line), $L_3 = 2.39$ m (black, dotted line). Note the differences in y-axis scale. (For interpretation of the references to colour in this figure legend, the reader is referred to the web version of this article.)

Table 4
Vertical locations of maximum pressure recordings on the front face of the structure. Bolded cells indicate the first trial in which waves broke on the specimen.

Trial	0.79 m	1.59 m	2.39 m
1	$z = 0.01$	$z = 0.01$	$z = 0.01$
2	$z = 0.01$	$z = 0.01$	$z = 0.01$
3	$z = 0.01$	$z = 0.01$	$z = 0.05$
4	$z = 0.05$	**$z = 0.15$**	**$z = 0.15$**
5	**$z = 0.05$**	$z = 0.15$	$z = 0.05$
6	$z = 0.01$	$z = 0.01$	$z = 0.01$
7	$z = 0.05$	$z = 0.05$	$z = 0.05$

However, it broke almost directly on the obstacle positioned at $L_2 = 1.59$ m. As the wave transformed from an unbroken wave at L_1 to a breaking wave at L_2, pressure increased from $p_1^* = 1.37$ to $p_2^* = 3.79$, an increase of 176%. Also note in Table 4 that the location of maximum pressure recorded by the specimen changed from near the base of the structure (local elevation 0.05 m above the flat beach) at L_1 to an elevation 0.15 m above the base of the structure at L_2, which was the highest elevated position of pressure gauges. When the specimen was positioned at $L_3 = 2.39$ m, this wave propagated past the obstacle as a turbulent bore and generated a pressure $p_3^* = 2.17$: less than that of the just-breaking wave at L_2 but still 59% larger than the unbroken wave pressure at L_1. Next, consider the wave of Trial 5 ($\eta^* = 0.64$), which broke over 0.8 m closer to shore, almost directly before the obstacle positioned at $L_1 = 0.79$ m. This wave, with a larger wave solitary fraction, induced a larger pressure at the structure at L_1 ($p_1^* = 4.49$) than waves that broke further inland. Note that this wave dissipated energy before impacting the obstacle positioned at L_2 or L_3; this dissipation due to wave breaking was reflected in a sharp drop in the pressure recorded on the instrumented specimen with respect to the offshore water surface perturbation for these two setback distances, as indicated in Fig. 10a. Thus, for houses positioned near the shoreline, breaking waves may induce larger forces than waves which break on inland structures. However, if waves break further inland, shoreward structures may not necessarily expect reduced pressures. Furthermore, wave breaking affects the vertical location of maximum pressure on a coastal structure; this spatial variation must be considered in the design of coastal residences.

While Fig. 10a reflects the maximum pressure with respect to the relatively constant offshore water surface perturbation, Fig. 10b shows the increasing contribution of dynamic wave impact to the maximum pressure with an increasing solitary wave fraction η^*. As η^* increased, the local water surface elevation decreased due to the wave breaking closer to the shoreline. The waves of Trials 6–7 propagated across the bare beach as low-elevation turbulent bores with water surface elevations 0.15–0.16 m at L_1, 0.09–0.10 m at L_2, and 0.06–0.07 m at L_3. The dimensionless pressure p^{**} with respect to these low water surface elevations increased greatly relative to the equivalent hydrostatic pressure at these locations. This is a significant finding because many design equations use the local bare-earth water surface elevation when estimating the maximum tsunami-induced pressures and forces on a structure. For example, the equation proposed by Asakura et al. (2000) and recommended by the JCO (2005) for tsunami design estimates the maximum pressure at a given elevation (z_i) above the ground (z_g) caused by a tsunami with no initial water level increase (e.g. $\eta_{flow} = 0$) as $p = \rho g(3\eta_{be} - z)$. For $z_i - z_g = 0$, solving for the dimensionless pressure p^{**} in the equation gives $p^{**} = p/\rho g(\eta_{be}) = 3$, indicating that p^{**} should converge to a value near 3 for a tsunami with characteristics of a solitary wave. While the equation produces conservative estimates for nonbreaking wave trials, Fig. 10b shows that the pressures measured for Trials 6 and 7 reach 10–20 times the hydrostatic approximation for the setback distances considered. Therefore, an idea of the wave characteristics (e.g. breaking or nonbreaking) or a consideration of wave-structure interaction must be incorporated into design to account for the contribution of impulsive wave pressures to the total structural

load. While Fig. 10b shows pressures much greater than the local hydrostatic pressures, Fig. 10a shows that the maximum pressure with respect to the total offshore water surface perturbation (p^*) was registered when waves broke on or just before the structure. After this maximum pressure, increasing the solitary wave ratio η^* decreased p^*. For the largest values of η^*, p^* converges to a value just above 3, which more closely matches the equation proposed by Asakura et al. (2000).

3.3. Setback distance effects

The three setback distances considered in configurations 1–3 were normalized by the offshore water surface perturbation to parameterize the setback distances considered here: $L_i^* = L_i / (\eta_{wave} + \eta_{flow})$. The effects of this normalized setback parameter are shown in Fig. 11, which plots p^* against L^* for the η^* corresponding to each trial of Table 2. Fig. 11 provides further evidence that unbroken waves, characterized by $\eta^* < 0.40$, do not produce large impulsive pressures on structures. However, turbulence and impact associated with wave breaking are identified as sharp spikes in maximum pressure and show that impulsive loading can induce critical pressures on a coastal structure. Fig. 11 shows sharp pressure peaks when wave breaking occurred closest to the obstacle; these conditions occurred for $L_1 = 0.79$ m ($L_1^* = 2.00$) at $\eta^* = 0.64$ (Trial 5) and for $L_2 = 1.59$ m ($L_2^* = 3.93$) at $\eta^* = 0.51$ (Trial 4). For both trials, positioning the specimen 0.80 m further inland resulted in decreased pressures for the same wave conditions. For example, experiments with $\eta^* = 0.64$ caused a maximum pressure $p^* = 4.49$ at L_1, but increasing the setback distance to 1.59 m for the same trial decreased the maximum pressure by 49% ($p^* = 2.29$). Therefore, estimation of tsunami force is highly sensitive to a structure's nearshore location, and the maximum pressure may be reduced when an obstacle is further removed from the breaking point of the first wave peak.

3.4. Macro-roughness effects

In addition to varying setback distance, nine structures were positioned in the 3×3 arrays shown in Fig. 6 to evaluate the effects of macro-roughness elements on wave transformation and maximum pressures. As shown in Fig. 6, two configuration variables were considered: (1) location of measurement specimen (first, second, or third row), and (2) spacing between obstacles (0.40 m or 0.20 m). Water surface elevation and pressure recordings for each trial were compared to those for unobstructed configurations. Fig. 12 compares water surface profiles with one structure and with nine structures at locations B1–B4 shown in Figs. 5 and 6. Specifically, the water surface elevations from configuration 1 were compared with those obtained from wave gauges in similar positions in macro-roughness tests from configurations 4 and 6 (0.2 m spacing) and configurations 7 and 9 (0.4 m spacing). The authors note slight differences (<0.2 m) in the exact distance from shoreline for wave gauge comparisons; however, differences in water surface elevation were due to structural interference with wave propagation, not overland wave dissipation. As shown in the figure, just offshore of the array of structures, the water surface profile is nearly identical to that in front of the unobstructed specimen; trials involving large pumping flow rates were characterized by greater flow reflection in macro-roughness configurations and thus greater water surface elevations in front of the array of structures. These observations echo those of Goseberg et al. (2008) who showed that modelled tsunami water levels were significantly increased in front of build environments. Between rows, the effects of macro-roughness elements on the water surface profile become apparent. In particular, behind the first row of obstacles, wave interaction with nearby structures increased the maximum water surface elevation, showing similar heights to those recorded in front of the array of structures. However, increasing rows of protection caused water surface dissipation. For the wave of Trial 7,
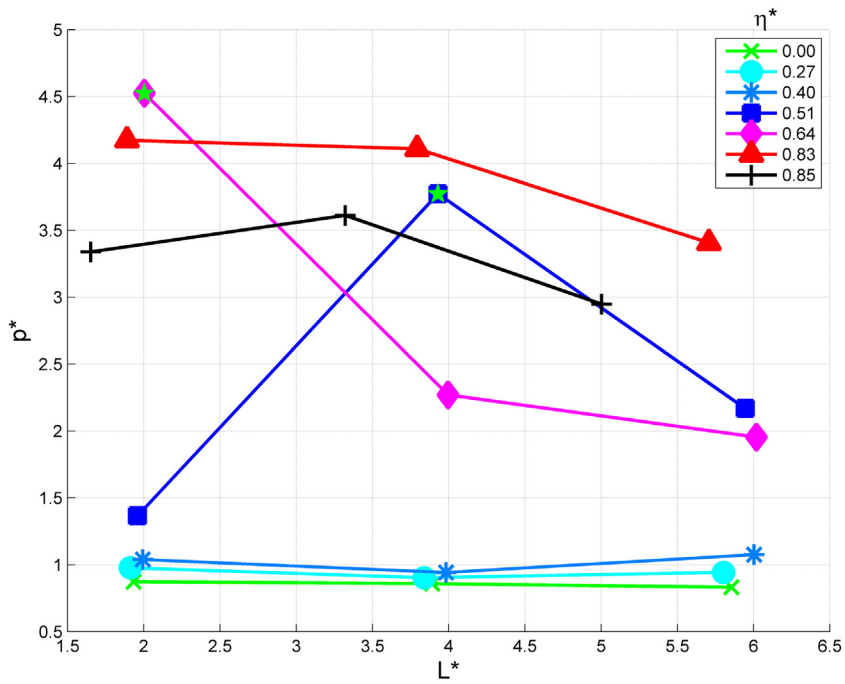
Fig. 11. Effects of setback distance and wave characteristics on maximum pressure: dimensionless pressure vs. nondimensional setback distance for each configuration, for the η^* conditions of Trials 1–7. Stars indicate conditions in which wave breaking occurred on or just before the structure [(2.00, 4.52) ($\eta^* = 0.64$) and (3.93, 3.77) ($\eta^* = 0.51$)].
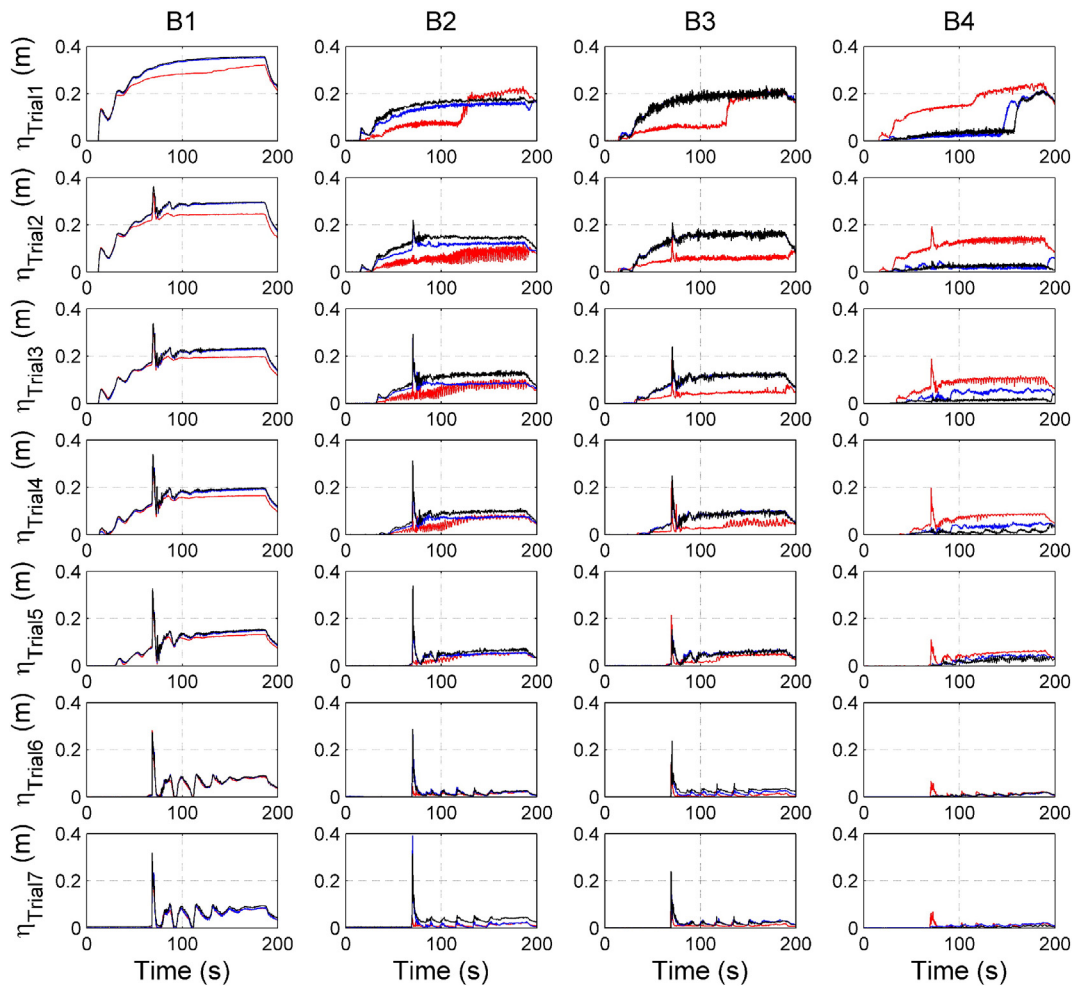

Fig. 12. Urban roughness effects on maximum water surface elevation for Trials 1–7 of Table 2. Locations (B1–B4) correspond with beach positions shown in Figs. 5 and 6. Blue line: 20 cm spaced array; black line: 40 cm spaced array; red line: unobstructed obstacle positioned 0.79 m from shore. (For interpretation of the references to colour in this figure legend, the reader is referred to the web version of this article.)

Table 5
Cross-shore, long-shore, and 2-D obstruction ratios defined by Goseberg (2013) for experimental configurations.

	0.40 m ($\psi_{ls} = 0.5$)		0.20 m ($\psi_{ls} = 0.67$)	
	ψ_{cs}	$\psi_{cs}\psi_{ls}$	ψ_{cs}	$\psi_{cs} = \psi_{ls}$
1 row shield	1.0	0.5	1.0	0.67
2 row shield	1.5	0.75	1.25	0.83
3 row shield	1.67	0.83	1.33	0.89

comparison of the water surface profiles shielded by one row (B2) indicates that the maximum water surface elevation was larger for the array with 0.20 m spacing (0.383 m) than for that with 0.40 m spacing (0.340 m). However, from location B2 to location B3 (behind two rows of structures), the maximum water surface elevations were reduced by 34.6% for the array spaced 0.40 m apart and by 57.4% for the array spaced 0.20 m apart. Therefore, while reduced spacing between obstacles may not change the water surface profile drastically for structures near the shoreline, the water surface may reduce more quickly with increasing lines of protection.

Goseberg (2013) identified two macro-roughness parameters to evaluate the change in long-wave run-up based on varied urban configurations: (1) the cross-shore obstruction ratio, ψ_{cs}, characterizing the effective obstruction length in the direction of inland propagating flow, and (2) a long-shore obstruction ratio, ψ_{ls}, giving the effective width of the macro-roughness. For the configurations tested here, long-shore and cross-shore obstruction ratios and their product (termed "2-D obstruction ratio") are given in Table 5, modified slightly with the note that the experimental configurations tested here did not extend across the entire width of the flume as in the experiments of Goseberg (2013). However, the macro-roughness characterization parameters are still useful. In particular, the 2-D obstruction ratio corroborates the analysis of Fig. 12: the configurations with 0.20 m spacing between elements were characterized by larger 2-D obstruction ratios than configurations with 0.40 m spacing. Narrower spacing between elements and increased inland distance (larger 2-D obstruction ratios) were

Table 6
Percent reduction of maximum pressure experienced by shielded specimen, compared to unobstructed cases at nearest setback distances. Bolded values of p* indicate the first case of wave breaking for each setback distance.

η^*	0.00	0.27	0.40	0.51	0.64	0.83	0.85
$p^*(L_1 = 0.79$ m)	0.87	0.98	1.04	1.36	**4.52**	4.17	3.34
$PR_1, a = 20$ cm, %	7.11	−0.19	−5.25	−6.54	28.34	2.20	−50.85
$PR_1, a = 40$ cm, %	23.54	32.25	−1.51	4.90	30.75	−10.54	−39.51
$p^*(L_2 = 1.59$ m)	0.86	0.90	0.94	**3.77**	2.27	4.11	3.61
$PR_2, a = 20$ cm, %	28.42	20.77	3.14	69.02	45.17	68.47	70.02
$PR_2, a = 40$ cm, %	26.36	12.60	17.72	51.96	33.52	67.69	53.35
$p^*(L_3 = 2.39$ m)	0.83	0.94	1.08	**2.17**	1.95	3.41	2.95
$PR_3, a = 20$ cm, %	19.93	36.13	23.96	57.66	52.73	72.44	71.28
$PR_3, a = 40$ cm, %	12.34	19.15	4.64	45.19	28.25	44.40	39.34

thus associated with increased water surface reductions behind additional rows of macro-roughness elements.

While Goseberg (2013) evaluated the effects of the macro-roughness ratios on reducing run-up, increased 2-D obstruction ratios were also found to change the maximum pressure caused by each wave case. Fig. 13 depicts the relationship between p^* and η^* for each spacing and location configuration, and Table 6 lists the percent reduction in pressure for urban roughness configurations, defined as:

$$PR_i = (p_{unobstructed,i} - p_{shielded,i})/p_{unobstructed,i} * 100\%, \tag{6}$$

where PR_i indicates the percent reduction in maximum pressure for the shielded specimen in the ith row with respect to the unobstructed specimen in the nearest setback position.

In the first row, the addition of structural elements did not shield the specimen from impact. However, the reflected wave energy from the obstacle to offshore was affected by adding structures, because additional obstacles reduced the transmission area of the propagating wave. Narrowing the gap between structures is expected to further increase local wave reflection. For rigid obstacles, the reflection and diffraction of waves due to structures may reduce the spatial variation of pressure compared to the single obstacle case. Assuming shoreward
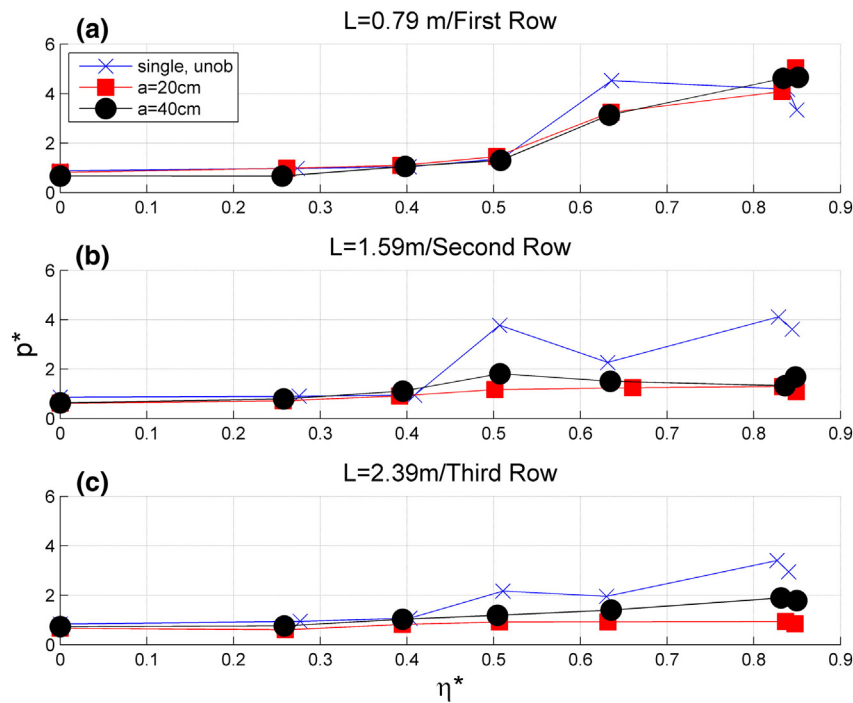

Fig. 13. Urban roughness effects on maximum pressure. Maximum pressure vs. solitary wave ratio: (a): front row; (b): 1.59 m setback or in second line of houses; (c): 2.39 m setback or in third line of houses. Blue lines (exes) indicate unobstructed case at appropriate location; red lines (squares) and black lines (circles) indicate 0.20 m and 0.40 m spacing between structures, respectively. (For interpretation of the references to colour in this figure legend, the reader is referred to the web version of this article.)

structures do not fail, more narrowly spaced configurations may be characterized by greater dissipation of breaking waves in the second and third rows but increased pressure in the first row of structures or in channels due to additional reflected wave energy and flow amplification.

Pressure reductions for shielded specimens were most apparent for breaking wave trials ($\eta^* > 0.51$). For nonbreaking waves (Trials 1, 2, and 3), maximum pressures recorded with macro-roughness elements were not significantly changed from unobstructed values: the frontal pressure measured when the obstacle was unobstructed or in the first row ranged from $p^* = 0.67$–1.09, while pressures in the second and third rows were between $p^* = 0.61$–1.11. In contrast, Table 6 indicates that after wave breaking occurred ($\eta^* \geq 0.51$), the maximum pressure exerted by the wave was greatly reduced in the second and third rows. For breaking wave cases, the maximum pressure experienced by a structure positioned behind one or two rows of houses was reduced by as much as 70% compared to the unobstructed case at the same set-back distance. Therefore, direct shielding by shoreward structures can significantly lessen the effects of breaking waves.

Fig. 13 and Table 6 also show the effect of varied spacing on pressure, reinforcing the relationship between the 2-D obstruction ratio and reduced tsunami run-up (Goseberg, 2013). Smaller spacing between obstacles effected a larger pressure reduction on directly shielded structures. For example, in the third row, the specimen experiencing a wave with $\eta^* = 0.83$–85 recorded a 40% pressure reduction compared to the unobstructed case when obstacles were spaced 0.40 m apart. Further decreasing the spacing between structures by 0.20 m caused a pressure reduction by over 70% for the same wave conditions. More narrowly spaced structures created less space in front of directly shielded structures for turbulent eddies to form, resulting in decreased frontal pressures. However, decreasing the spacing between obstacles increased water velocities in the side streets and maximum pressures on structures in the front row due to reduced flow area and additional reflected wave energy. For this reason, structures not directly shielded from wave propagation may experience larger forces in urban environments (Park et al., 2013). Seawalls that can withstand increased wave energy from oblique directions may be useful as a first line of defense against hurricane or tsunami wave forces.

4. Summary and conclusions

4.1. Model successes, limitations and areas for future study

The experiments presented in this work show the functionality of the Hybrid Tsunami Flume at Ujigawa Laboratory in creating complex wave conditions similar to those observed during the 2011 Tohoku Earthquake Tsunami, characterized by a solitary wave profile superimposed on a longer period water surface rise. Effects of macro-roughness elements in reducing critical pressures on a shielded specimen are also explored. The work here provides insight into important relationships between offshore wave conditions, onshore macro-roughness configurations, and wave-structure interactions; however, experimental limitations and idealizations must be addressed so that future experiments can continue to refine the state-of-the-art in physical modelling of tsunami hydrodynamics.

One limitation of the current experiment is the idealization of the typical Japanese house as a rigid rectangular prism. As discussed above, the specimen was weighted to the bottom with sufficient weight to prevent movement due to the wave impact; thus only horizontal loads are considered in this study. A real tsunami will generate horizontal loads as well as vertical loads on the underside of structures; many homes in the inundation region during the 2011 Tohoku Earthquake Tsunami were washed away due to the tsunami wave (Gokon and Koshimura, 2012). Likely, the combination of the horizontal impact force and vertical buoyant forces caused these failures. Further, upon failure, a home will become a threat to shoreward homes due to

potential debris impact. Debris impact was not considered in experiments; however strong foundation connections and consideration for uncertainty due to debris loading will be considered in future experiments.

Another consideration is the physical model's ability to represent a prototype tsunami. Comparisons with GPS data obtained from the 2011 Tohoku Earthquake Tsunami indicate that experimental measurements successfully represented the tsunami profiles of GB801 and GB803 (Kawai et al., 2013). However, as Madsen et al. (2008) showed, the short period solitary wave does not accurately represent the time scale of a real-world tsunami. While this work addresses new data that has shown short period waves embedded in a longer-scale water level rise, the mechanically-generated wave still scales to a prototype time shorter than those of real tsunamis. However, tsunami design is regulated by tsunami water level without consideration of the total period and time-dependent load, and video analysis of the Tohoku Earthquake Tsunami showed that the first impact of the tsunami wave on the building's wall could be extremely strong and cause structural failure. Therefore, creating similar maximum wave heights using a combination of wave generation mechanisms marks a step forward in physical modelling of complex real-world events. Future experiments will focus on additional combinations of pump-generated flow and mechanically-generated waves to test the facility's ability in generating longer period waves.

Finally, laboratory experiments and numerical models seek to better understand tsunami onshore propagation in order to ultimately design structures to resist tsunami and wave-induced forces. However, design codes that present equations for estimating the maximum force on a structure often must make simplifying assumptions about the maximum tsunami-induced pressure. Therefore, understanding of extreme pressures is an essential starting point for coastal engineers in estimating wave impact loads and the effects of macro-roughness in reducing these loads. Further, extreme pressures must be considered when designing a structure to prevent local damage. Much work has been done to estimate wave-induced forces on structures (e.g. Morison et al., 1950; Ramsden, 1993; Bradner et al., 2009; Fujima et al., 2009; Al-Faesly et al., 2012; Thomas and Cox, 2012; Kihara et al., 2015). While detailed analysis of forces caused by the waves generated in the current experiment and their application to design guidelines is beyond the scope of this work, full integrations of pressure measurements are the subject of current study and will be used to examine the reliability of design equations (e.g. JCO, 2005; ASCE, 2016).

4.2. Overall conclusions

Benchmark experiments indicated that the maximum pressure experienced by structural elements was significantly affected by wave characteristics, wave breaking, and setback distance. Major conclusions from this analysis are threefold:

1. When waves broke on or just before a structure, the maximum pressure recorded on the front face of the specimen more than tripled when compared to that caused by nonbreaking waves. The position of wave breaking itself was affected by the ratio of solitary wave height to total water surface disturbance; this variable, combined with a structure's setback distance from shoreline, can greatly impact the maximum pressure exerted on a structure during a tsunami.

2. As waves approached a pure solitary wave ($\eta^* = 1$), maximum pressures predicted by the tsunami design equation recommended by the Japanese Cabinet Office underestimated measured values when using the bare-earth water surface elevation (Asakura et al., 2000; JCO, 2005). However, estimates were conservative for nonbreaking wave trials, and inputting the total offshore water surface perturbation into the design equation resulted in good agreement between predicted and experimental pressures for breaking wave conditions. Design equations may be conservatively applied in the field and must

be further investigated for their application to waves with varying offshore characteristics.

3. The maximum pressure caused by breaking waves decreased by 40–70% when one or two rows of obstacles shielded the instrumented specimen. If a seaward structure does not fail, design standards may consider conservative reduction factors for structures located behind two or more rows of obstacles when estimating maximum tsunami pressure.

In practice, a coastal engineer must account for case-specific parameters associated with local bathymetry, community layout, and offshore wave characteristics. Therefore, pressures measured here may not directly apply to structural design criteria for coastal residences. However, in all experiments, critical pressures were generated by breaking waves, and shielding elements consistently reduced the maximum pressure for breaking wave trials. Protective structures that can withstand tsunami wave-induced forces such as breakwaters, seawalls, reinforced dunes, and reinforced concrete buildings (e.g. car parking lot) along the ocean-front are recommended to mitigate damage.

Acknowledgements

References

Al-Faesly, T., Palermo, D., Nistor, I., Cornett, A., 2012. Experimental modeling of extreme hydrodynamic forces on structural models. Int. J. Prot. Struct 3 (4), 477–505.

Asakura, R., Iwase, K., Iketani, T., 2000. Proc. Coast. Eng. JSCE 47, 911–915.

ASCE, 2016. Minimum design loads for buildings and other structures: chapter 6 tsunami loads and effects. ASCE/SCI 7-16. York, New.

Baldock, T.E., Cox, D., Maddux, T., Killian, J., Fayler, L., 2009. Kinematics of breaking tsunami wave fronts: a data set from large scale laboratory experiments. Coast. Eng. 2009, 506–516.

Blake, E.S., Kimberlain, T.B., Berg, R.J., Cangialosi, J.P., Beven II, J.L., 2013. Tropical Cyclone Report: Hurricane Sandy (AL 182012), 22–29 October 2012. National Hurricane Center, pp. 1–157.

Bradner, C., Schumacher, T., Cox, D., Higgins, C., 2009. Large scale laboratory measurements of wave forces on highway bridge superstructures. Proceedings of the 31st International Conference, Hamburg, Germany, pp. 3554–3566.

Bremm, G.C., Goseberg, N., Schlurmann, T., Nistor, I., 2015. Long wave flow interaction with a single square structure on a sloping beach. J. Mar. Sci. Eng 3, 821–844.

Bricker, J.D., Gibson, S., Takagi, H., Imamura, F., 2015. On the need for larger Manning's roughness coefficients in depth-integrated tsunami inundation models. Coast. Eng. J 1–13.

Briggs, M.J., Synolakis, C.E., Harkins, G.S., Green, D.R., 1995. Laboratory experiments of tsunami runup on a circular island. Pure Appl. Geophys 144 (3–4), 569–593.

Bullock, G.N., Obhrai, C., Peregrine, D.H., Bredmose, H., 2007. Violent breaking wave impacts. Part 1: results from large-scale regular wave tests on vertical and sloping walls. Coast. Eng 54 (2007), 602–617.

Chanson, H., Aoki, S.I., Maruyama, M., 2003. An experimental study of tsunami runup on dry and wet horizontal coastlines. Sci. Tsunami Haz 20 (5), 278–293.

Chen, C.Y., Hsu, J.R., Chen, H., Kuo, C., Cheng, M., 2007. Laboratory observations on internal solitary wave evolution on steep and inverse uniform slopes. Ocean Eng 34, 157–170.

Cooker, M.J., 2002. Liquid impact, kinetic energy loss and compressibility: Lagrangian, Eulerian, and acoustic viewpoints. J. Eng. Math 44, 259–276.

Cooker, M.J., Peregrine, D.H., 1995. Pressure impulse theory for liquid impact problems. J. Fluid Mech 297, 193–214.

Cox, D., Tomita, T., Lynett, P., Holman, R., 2008. Tsunami inundation with macro-roughness in the constructed environment. Proceedings of the 31st International Conference on Coastal Eng., pp. 1421–1432

Dietrich, J.C., Tanaka, S., Westerink, J.J., Dawson, C.N., Jr, L., Zijlema, M., Holthuijsen, L.H., Smith, J.M., Westerink, L.G., Westerink, H.J., 2012. Performance of the unstructured-

mesh, SWAN + ADCIRC model in computing hurricane waves and surge. J. Sci. Comput 52, 468–497.

Fanelli, C., Fanelli, P., Wolcott, D., 2013. NOAA Water Level and Meteorological Data Report: Hurricane Sandy. United States Department of Commerce, Silver Spring, MD.

Fujima, K., Achmad, F., Shigihara, Y., Mizutani, N., 2009. Estimation of tsunami force acting on rectangular structures. J. Disaster Res 4 (6), 404–408.

Gokon, H., Koshimura, K., 2012. Mapping of building damage of the 2011 Tohoku Earthquake Tsunami in Miyagi Prefecture. Coast. Eng. J 54 (1), 1–12.

Goseberg, N., 2013. Reduction of maximum tsunami run-up due to the interaction with beachfront development - application of single sinusoidal waves. Nat. Hazards Earth Syst. Sci. 13, 2991–3010.

Goseberg, N., Schlurmann, T., 2012. Interaction of idealized urban infrastructure and long waves during run-up and on-land flow process in coastal regions. Proceedings of 33rd Conference on Coastal Eng., Santander, Spain.

Goseberg, N., Stahlmann, A., Schimmels, S., Schlurmann, T., 2008. Highly resolved numerical modelling of tsunami run-up and inundation scenarios in the city of Padang, West Sumatra. Poster Proceedings of the International Conference on Coastal Eng, p. 2008.

Goseberg, N., Wurpts, A., Schlurmann, T., 2013. Laboratory-scale generation of tsunami and long waves. Coast. Eng. 79, 57–74.

Goto, C., Shuto, N., 1983. Effects of large obstacles on tsunami inundations. In: Iida, K., Iwasaki, T. (Eds.), Tsunamis: Their Science and Engineering. Terra Science Pub. Co., Tokyo/Reidel, Dordrecht, pp. 515–525 chap. Tsunami Run-up.

Hattori, M., Arami, A., Yui, T., 1994. Wave impact pressure on vertical walls under breaking waves of various types. Coast. Eng. 22 (1–2), 79–114.

Holthuijsen, L.H., Booij, N., Ris, R.C., 1993. A spectral wave model for the coastal zone. Proceedings 2nd International Symposium on Ocean Wave Measurement and Analysis, New Orleans, Louisiana, July 23–28, 1993, New York, pp. 630–641.

Irish, J., Weiss, R., Yang, Y., Song, Y.K., Zainali, A., Marivela-Colmenarejo, R., 2014. Laboratory experiments of tsunami run-up and withdrawal in patchy coastal forest on a steep beach. Nat. Hazards 74, 1933–1949.

JCO/Task Committee Under the Japanese Cabinet Office, 2005. Design guidelines for tsunami shelters (in Japanese). http://www.bousai.go.jp/oshirase/h17/tsunami_siryo2.pdf.

JCO: Japanese Cabinet Office, 2011. Off the Pacific Ocean earthquake and resulting tsunamis: chapter III - disaster damage in Japan from the Tohoku District. Prime Minister's Official Residence. pp. III-1–III-23.

Jelesnianski, C.P., Chen, J., Shaffer, A., 1992. SLOSH: sea, lake, and overland surges from hurricanes. NOAA Technical Report NWS 48. National Oceanic and Atmospheric Administration, US Department of Commerce, pp. 1–71.

Kawai, H., Satoh, M., Kawaguchi, K., Seki, K., 2012. Recent tsunamis observed by GPS buoys off the Pacific coast of Japan. Coast. Eng. Proc. 33, 1–15.

Kawai, H., Satoh, M., Kawaguchi, K., Seki, K., 2013. Characteristics of the 2011 Tohoku Tsunami waveform acquired around Japan by NOWPHAS equipment. Coast. Eng. J 55 (4), 1350009.

Kazama, M., Noda, T., 2012. Damage statistics (summary of the 2011 off the Pacific coast of Tohoku earthquake damage). Soils Found. 52 (5), 780–792.

Kihara, N., Niida, Y., Takabatake, D., Kaida, H., Shibayama, A., Miyagawa, Y., 2015. Large-scale experiments on tsunami-induced pressure on a vertical tide wall. Coast. Eng. 99, 46–63.

Koshimura, S., Oie, T., Yanagisawa, H., Imamura, F., 2009. Developing fragility functions for tsunami damage estimation using numerical model and post-tsunami data from Banda Aceh, Indonesia. Coast. Eng. J 51 (3), 243–273.

Lackey, M., 2011. National Climatic Data Center. 2011. Billion dollar US/climate disasters [data file]. Retrieved from http://www.ncdc.noaa.gov/img/reports/billion/disasters2010.pdf.

Leone, F., Lavigne, F., Paris, R., Denain, J.C., Vinet, F., 2011. A spatial analysis of the December 26th, 2004 tsunami-induced damages: lessons learned for a better risk assessment integrating buildings vulnerability. Appl. Geogr. 31 (1), 363–375.

Liu, P.L.F., Cho, Y.S., Briggs, M.J., Kanoglu, U., Synolakis, C.E., 1995. Runup of solitary waves on a circular island. J. Fluid Mech 302 (1), 259–285.

Luettich Jr., R.A., Westerink, J.J., Scheffner, N.W., 1992. ADCIRC: an advanced three-dimensional circulation model for shelves coasts and estuaries, report 1: theory and methodology of ADCIRC-2DDI and ADCIRC-3DL. Dredging Research Program Technical Report DRP-92-6, US Army Engineers Waterways Experiment Station, Vicksburg, MS, pp. 1–137.

Lynett, P., Wu, T., Liu, P., 2002. Modeling wave runup with depth-integrated equations. Coast. Eng. 46, 89–107.

Lynett, P., Liu, P., Sitanggang, K., Kim, D., 2008. Modeling wave generation, evolution, and interaction with depth-integrated, dispersive wave equations. COULWAVE Code Manual. Cornell University Long and Intermediate Wave Modeling Package 2.0, pp. 1–90.

Ma, G., Shi, F., Kirby, J.T., 2012. Shock-capturing non-hydrostatic model for fully dispersive surface wave processes. Ocean Model 43-44, 22–35.

Madsen, P.A., Fuhrman, D.R., Schaffer, H.A., 2008. On the solitary wave paradigm for tsunamis. J. Geophys. Res 113, C12012. http://dx.doi.org/10.1029/2008JC004932.

McLachlan, A., Dorvlo, A., 2005. Global patterns in sandy beach microbenthic communities. J. Coast. Res 21 (4), 674–687.

Mimura, N., Yasuhara, K., Kawagoe, S., Yokoki, H., Kazama, S., 2011. Damage from the Great East Japan Earthquake and Tsunami - a quick report. Mitig. Adapt. Strateg. Glob. Chang. 16 (7), 803–818.

Mori, N., Takahashi, T., 2012. Nationwide post event survey and analysis of the 2011 Tohoku Earthquake Tsunami. Coast. Eng. J 54 (1), 1250001.

Mori, N., Takahashi, T., Yasuda, T., Yanagisawa, H., 2011. Survey of 2011 Tohoku earthquake tsunami inundation and run-up. Geophys. Res. Lett 38 (7), L00G14.

Mori, N., Kato, M., Kim, S., Mase, H., Shibutani, Y., Takemi, T., Tsuboki, K., Yasuda, T., 2014. Local amplification of storm surge by Super Typhoon Haiyan in Leyte Gulf. Geophys. Res. Lett. 41 (14), 5106–5113.

Morison, J.R., O'Brien, M.P., Johnson, J.W., Schaaf, S.A., 1950. The forces exerted by surface waves on piles. Pet. Trans 189, 149–157.

Nandasena, N.A.K., Sasaki, Y., Tanaka, N., 2012. Modeling field observations of the 2011 Great East Japan Tsunami: efficacy of artificial and natural structures on tsunami mitigation. Coast. Eng. 67, 1–13.

Nicholls, R.J., Small, C., 2002. Improved estimates of coastal population and exposure to hazards released. Eos Trans. AGU 83 (28), 301–305.

NOWPHAS: Nationwide Ocean Wave Information for Ports and Harbours, 2011A. Tohoku Earthquake Tsunami GPS Buoy Data. Port and Airport Research Institute (PARI), Yokosuka, Japan 11 March.

ODOT: Oregon Department of Transportation, 2014. Appendix A - hydraulic roughness (Manning's n) values of conduits and channels. ODOT Hydraulics Manual, Salem, OR.

Oshnack, M.E., Aguiniga, F., Cox, D., Gupta, R., van de Lindt, J., 2009. Effectiveness of small onshore seawalls in reducing forces induced by tsunami bore: large scale experimental study. J. Disaster Res 4 (6), 382–390.

Oumeraci, H., Klammer, P., Partenscky, H.W., 1993. Classification of breaking wave loads on vertical structures. J. Waterw. Port Coast. Ocean Eng 119 (4), 381–397.

Papadopoulos, G.A., Caputo, R., McAdoo, B., Pavlides, S., Karasthis, V., Fokaefs, A., Orfanogiannaki, K., Valkaniotis, S., 2006. The large tsunami of 26 December 2004: field observations and eyewitnesses accounts from Sri Lanka, Maldives Is. and Thailand. Earth Planets Space 58 (2), 233–241.

Park, H., Cox, D.T., Lynett, P.J., Wiebe, D.M., Shin, S., 2013. Tsunami inundation modeling in constructed environments: a physical and numerical comparison of free-surface elevation, velocity, and momentum flux. Coast. Eng. 79 (2), 9–21.

Peregrine, D.H., 2003. Water wave impacts on walls. Annu. Rev. Fluid Mech 35, 23–43.

Ramsden, J.D., 1993. Tsunamis: Forces on a Vertical Wall Caused by Long Waves, Bores, and Surges on a Dry Bed PhD Thesis California Institute of Technology, Pasadena, California.

Reis, A.H., Gama, C., 2010. Sand size versus beachface slope - an explanation based on the constructal law. Geomorphology 114, 276–283.

Robertson, I.N., Riggs, H.R., Yim, S.C., Young, Y.L., 2007. Lessons from Hurricane Katrina storm surge on bridges and buildings. J. Waterw. Port Coast. Ocean Eng.-ASCE 133, 463–483.

Rossetto, T., Allsop, W., Charvet, I., Robinson, D.I., 2011. Physical modelling of tsunami using a new pneumatic wave generator. Coast. Eng. 58 (6), 517–527.

Small, C., Nicholls, R.J., 2003. A global analysis of human settlement in coastal zones. J. Coast. Res 19 (3), 584–599.

Suppasri, A., Mas, E., Koshimura, S., Imai, K., 2012. Developing tsunami fragility curves from the surveyed data of the 2011 Great East Japan Tsunami in Sendai and Ishinomaki Plains. Coast. Eng. J 54, 1–16.

Suppasri, A., Shuto, N., Imamura, F., Koshimura, S., Mas, E., Yalciner, A.C., 2013a. Lessons learned from the 2011 Great East Japan Tsunami: performance of tsunami countermeasures, coastal buildings, and tsunami evacuation in Japan. Pure Appl. Geophys. 170 (2013), 993–1018.

Suppasri, A., Mas, E., Charvet, I., Gunasekera, R., Imai, K., Fukutani, Y., Abe, Y., Imamura, F., 2013b. Building damage characteristics based on surveyed data and fragility curves of the 2011 Great East Japan tsunami. Nat. Hazards 66, 319–341.

Synolakis, C.E., 1987. The runup of solitary waves. J. Fluid Mech 185, 523–545.

Tajima, Y., Yasuda, T., Pacheco, B.M., Cruz, E.C., Kawasaki, K., Nobuoka, H., Miyamoto, M., Asano, Y., Arikawa, T., Ortigas, N.M., 2014. Initial report of JSCE-PICE joint survey on the storm surge disaster caused by Typhoon Haiyan. Coast. Eng. J 56 (1), 1450006.

Thomas, S., Cox, D., 2012. Influence of finite-length seawalls for tsunami loading on coastal structures. J. Waterw. Port Coast. Ocean Eng 138 (3), 203–214.

Thomas, S., Killian, J., Bridges, K., 2015. Influence of macroroughness on tsunami loading of coastal structures. J. Waterw. Port Coast. Ocean Eng 141, 1.

Tomiczek, T., Kennedy, A., Rogers, S., 2014. Collapse limit state fragilities of wood-framed residences from storm surge and waves during Hurricane Ike. J. Waterw. Port Coast. Ocean Eng 140 (1), 43–55.

Tomiczek, T., Kennedy, A., Zhang, Y., Owensby, M., Hope, M.E., Lin, N., Flory, A., 2016. Hurricane damage classification methodology and fragility functions derived from Hurricane Sandy's effects in coastal New Jersey. J. Waterw. Port Coast. Ocean Eng resubmitted.

Tomita, T., Honda, K., 2009. Tsunami estimation including effect of coastal structures and buildings by 3D model. Coastal Structures '07.

Tomita, T., Honda, K., Kakinuma, T., 2006. Application of three-dimensional tsunami simulator to estimation of tsunami behavior around structures. Int. Conf. on Coastal Eng., San Diego.

Tsuji, Y., Namegaya, Y., Matsumoto, H., Iwasaki, S.I., Kanuba, W., Sriwachai, M., Meesuk, V., 2006. The 2004 Indian tsunami in Thailand: surveyed runup heights and tide gauge records. Earth Planets Space 58 (2), 223–232.

Udo, K., Sugawara, D., Tanaka, H., Imai, K., Mano, A., 2012. Impact of the 2011 Tohoku Earthquake and Tsunami on beach morphology along the Northern Sendai Coast. Coast. Eng. J 54 (1), 1250009.

van de Lindt, J.W., Graettinger, A., Gupta, R., Skaggs, T., Pryor, S., Fridley, K.J., 2007. Performance of wood-frame structures during Hurricane Katrina. J. Perform. Constr. Facil 21 (2), 108–116.

van de Lindt, Gupta, R., Garcia, R.A., Wilson, J., 2009. Tsunami bore forces on a compliant residential building model. Eng. Struct 31 (2), 2534–2539.

Wei, G., Kirby, J.T., 1995. A time-dependent numerical code for extended Boussinesq equations. J. Waterw. Port Coast. Ocean Eng 120, 251–261.

Westerink, J.J., Luettich, R.A., Feyen, J.C., Atkinson, J.H., Dawson, C., Roberts, H., Powell, M.D., Dunion, J.P., Kubatko, E.J., Pourtaheri, H., 2008. A basin- to channel-scale unstructured grid hurricane storm surge model applied to southern Louisiana. Mon. Weather Rev. 136 (3), 833–864.

Wood, D.J., Peregrine, D.H., Bruce, T., 2000. Wave impact on a wall using pressure-impulse theory. I: Trapped air. J. Waterw. Port Coast. Ocean Eng 126 (4), 182–190.

Yeh, H., 2009. In: Bernard, E.N., Robinson, A.R. (Eds.), Tsunami Impacts on Coastlines. The Sea: Tsunamis. Harvard University Press, Cambridge, pp. 333–370.